Effects on cavitation inception of leading and trailing edge flaps on a high-performance hydrofoil

Fatiha Mohammed Arab [a], Benoît Augier [b], François Deniset [a], Pascal Casari [c], Jacques André Astolfi [a,*]

[a] French Naval Academy Research Institute (IRENav), EA 3634, 29240 Brest, France
[b] IFREMER, RDT, F-29280 Plouzané, France
[c] Research Institute in Civil Engineering and Mechanics—GeM, 44606 Saint-Nazaire, France

Keywords:
Hydrofoil
High performance
Morphing
Cavitation
Flaps

A B S T R A C T

For high-performance foiling yachts, cavitation is often a limiting factor for take-off and top speed. The present work investigates solutions to control the onset of cavitation thanks to a combination of leading edge and trailing edge flaps. Numerical and experiments in a hydrodynamic tunnel are conducted in order to assess the effect of specific geometric parameters on the hydrodynamic performance and cavitation inception. The hydrofoils are manufactured using an additive 3D printing technique and tested in the cavitation tunnel of IRENav at an inflow velocity of 6.67 m/s ($Re = 10^6$). The effect on the hydrodynamic performances and cavitation buckets of a 70% chord trailing edge flap and a 20% chord leading edge flap of NACA 0012 is investigated. The results show that the lift coefficient increases and the cavitation bucket shifts up and decreases with the flaps deflection. The experimental results are in good agreement with the numerical ones by highlighting the capacity of the flaps to modify both the operating domain and the cavitation bucket of the hydrofoil. Eventually, the PLA 3D printed foils prove to be a fast, unexpensive and reliable technologies for cavitation studies.

1. Introduction

If new hydrofoil technologies used on sailing boats are intended to improve the hydrodynamic forces, cavitation is often a limiting factor for take-off and top speed.

Using this new concept of hydrofoils allow the control of the lift and drag forces for various operating conditions, but it can lead to cavitation onset at high speed and moderate angles of incidence but also at low speed and high angles. Improving the hydrodynamic performances and delaying the cavitation inception requires the modification of shape, hence the idea of using morphing hydrofoils. Morphing structures could be an interesting way to adapt the performance to different operating regimes (Weisshaar, 2013).

The use of morphing structures is particularly considered in aerodynamic applications including flying performance (Guo, 2020). Jawahar et al. (2018) analyzed experimentally and numerically the effect of camber flaps on the pressure distribution, on the lift and drag forces as well as the effect on the wake flow. They concluded that the camber of flaps significantly affects the aerodynamic performance and the downstream wake development of the airfoil. The increase of the camber flap profiles increases the lift coefficients and reduces the lift-to-drag ratio. The aerodynamic performance and mechanical properties of a flexible suction side of an airfoil powered by two actuators are numerically investigated by Brailovski et al. (2008).

The gap present at the spanwise ends of the control surfaces is one of the sources of noise and drag. Woods et al. (2016) have replaced this gap by a smooth, three-dimensional morphing transition section that elastically lofts between the rigid wing and the moving control surface in a passive and continuous manner. The passive control of this compliant morphing flap transition has the advantage of increasing the lift and reducing the drag. The effect of various variable camber continuous trailing edge flap (VCCTEF) on the lift and drag forces is discussed by Kaul and Nguyen (2018). It was noted that the best stall performance (L/D) was demonstrated by the circular and parabolic arc camber flaps. In a review, Barbarino et al. summarized shape-changing technologies for fixed and rotary wings and highlighted the need for further research on skins, actuators/mechanisms and control theories (Barbarino et al., 2011).

Most objectives of hydrodynamic applications are similar to those of aerodynamics. The airfoil technology can be then used in the design

* Corresponding author.
E-mail address: jacques-andre.astolfi@ecole-navale.fr (J.A. Astolfi).

https://doi.org/10.1016/j.apor.2022.103285

of the hydrofoil by taking the differences between the fluid properties and the cavitation phenomena into account .

To meet hydrodynamic requirements, adaptive composites are used in many marine technologies including propulsive devices, underwater vehicles and propellers. In Young et al. (2016), the authors summarized the progress on the numerical modeling, the experimental studies, design and optimization of adaptive composite marine propulsors and turbines.

In order to assess the effect of cavitation on the structural response, Ducoin et al. (2012) have studied the displacement of a flexible homogeneous POM hydrofoil in a cavitating flow. They found that the hydrodynamic loading unsteadiness increases vibrations experienced by the hydrofoil. Numerically, Garg et al. (2016), Garg et al. (2017), Garg et al. (2015) have developed a shape optimization tool to predict the hydrodynamic performance including cavitation inception conditions. The predicted hydrodynamic coefficients (C_L, C_D, and C_M) and the tip bending deflections are compared to experimental results obtained by Garg et al. (2019). Numerical results concur with measured values for both the baseline and the optimized hydrofoils across a wide range of lift conditions.

In order to control lift generated by hydrofoils on boats, Giovannetti et al. (2018) have numerically and experimentally analyzed hydrofoil geometry designed to reduce the lift coefficient passively by increasing the flow velocity. This study was achieved through the use of wind tunnel experiments including displacements measurements, which concurred with the numerical results. They found that twist deformations resulted in a reduction in the effective angle of attack by 30% at higher flow velocities, which significantly reduced the foil's lift and drag.

The performance of hydrofoils can be limited by the phenomenon of cavitation. Of the various cavitation phenomena on a hydrofoil section, cloud cavitation is distinctly periodic and accompanying strong vibration, noise and erosion as it was mentioned by Kawanami et al. (1997). These latter have investigated cloud cavitation in a series of experiments and observations. They have used high-speed videos and cameras as well as pressure measurements by pressure pick-ups and hydrophones. They established a relationship between the re-entrant jet and the cloud cavity generation process and they confirm the essential role of the re-entrant jet in the onset of cloud cavitation.

The passive flow control techniques to control the cavitation are discussed by Zaresharif et al. in Zaresharif et al. (2021) among these techniques, we find :

- The passive flow control methods in delaying boundary layer separation and to reduce the cavity length and cavitation growth.
- The generation of streamwise vortices and reduction in boundary layer spanwise non-uniformities.
- The transfer high momentum fluid from the free stream flow moved to the near-wall low energy region and moving higher kinetic energy flow to the surface's vicinity.
- Declining pressure gradient and intensity of pressure fluctuation at the separation point and increasing resistance against pressure rise before boundary layer separation.
- The re-entrant jets play an important role in cavitation, the effect of passive flow control was weakening the re-entrant jets and their penetration depth and suppressing the propagation of the pressure wave of collapse.

The French Naval Academy Research Institute (IRENav) is interested in the study of deformed hydrofoils, their responses and enlarging their operating domain. Experimentally, the Fluid–Structure Interaction has been investigated by studying the structural response of a flexible lightweight hydrofoil undergoing various flow conditions including cavitating flow by Lelong et al. (2018), Lelong et al. (2016). An optimization of design and elastic characteristics of a hydrofoil equipped with deformable elements providing flexibility to the trailing edge was developed by Sacher et al. (2018). In their study, Arab et al. (2019) analyzed experimentally and numerically the effect of an imposed internal pressure of a compliant composite hydrofoil. It is shown that pressure driven compliant composite structure allows to enlarge the operational domain of the compliant hydrofoil. Also, they found that cavitation can be controlled to some extent by changing only the internal pressure for a given angle of attack and a given inflow velocity. Vanilla et al. studied the fluid–structure interaction effect of bend twist coupling on hydrodynamic performance (Vanilla et al., 2021). They developed numerical approaches based on the FSI coupling algorithm and they compared the results to experimental ones obtained in the hydrodynamic tunnel.

Research studies begin to focus on the effect of the geometric parameters of hydrofoils in order to enlarge their non-cavitation domain. Ladino (2011) conducted a numerical study using XFOIL software to investigate the effect of geometric parameters of NACA 4 series profiles on the cavitation characteristics. He evaluated the effect of camber percentage, camber location and maximum thickness. He also analyzed the effect of trailing edge deflection on the cavitation bucket. Results show that increase of thickness enlarges the non-cavitation domain. The same remark is noted for camber increment, especially at high angles of attack. Simulations show that the increasing camber and trailing edge deflection induce to the non cavitation bucket to move to high lift zone. In another study, the adverse effects of cavitation and roughness are taken into account by Sun et al. (2020). They developed an algorithm to optimize geometric parameters of a NACA 2415 in order to affect lift and drag coefficient as well as the minimum pressure coefficient. Other studies are based on the optimization of the propeller geometry as the work of Gaggero et al. (2016). Their study aimed at evaluating the performance of propellers selected by a genetic optimization algorithm including cavitation criteria.

The present paper presents an experimental and numerical study where the effect of leading and trailing edge deflections of a hydrofoil is investigated. The effect of the leading and trailing edge flaps on hydrodynamic performance is predicted using Xfoil software. Then, four hydrofoils taking advantage of design solution based on 3D printing at moderate cost compared to the high cost usual Inox steel manufacturing and tested in the cavitation tunnel. These experiments aim to validate the numerical tool in order to be able to use it to evaluate the effect of the geometric parameters of a foil on its performance.

The paper describes the experimental setup, the numerical computations and presents the main results.

2. Experimental setup

Experiments are carried out in the cavitation tunnel at IRENav (Fig. 1). The tunnel test section is 1 m length with a square section of 0.192 m side. The inflow velocity ranges between 0.5 and 15 m/s. The pressure in the tunnel test section ranges between 0.1 bar and 3 bar to control the cavitation which is given by a cavitation number defined by Eq. (1) and the measured turbulence intensity in the test section is 2% at 5 m/s. This cavitation number can therefore be compared to the opposite of pressure coefficient $-C_{pmin}$ defined as the minimum of pressure coefficient (Eq. (2)).

$$\sigma = \frac{P_{ref} - P_v}{\frac{1}{2}\rho V^2} \tag{1}$$

$$C_p = \frac{P - P_{ref}}{\frac{1}{2}\rho V^2} \tag{2}$$

Where P_{ref} is the reference pressure in the test section, P_v is the vapor pressure at the water temperature, P is the local pressure, V is the inflow velocity, and ρ is the water density. Thus, when $\sigma < -C_{pmin}$, that is to say when $P < P_v$, cavitation is expected to appear in the flow at the point where the pressure coefficient is the lowest.

Four 0.15 m chord hydrofoils are manufactured using an additive manufacturing process based on 3D printing techniques (PLA material)

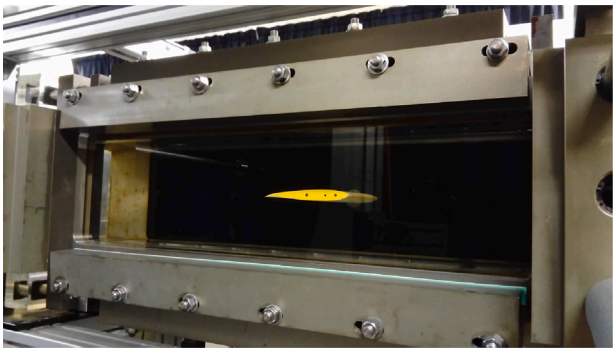

Fig. 1. Hydrodynamic tunnel test section at IRENav with the NACA 0012 profile clamped on the opposite vertical wall.

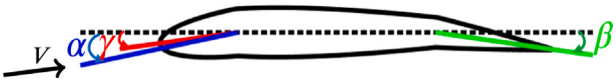

Fig. 2. Schematic diagram of the different angles: angle of incidence (α), angle of the leading edge flap (γ) and angle of the trailing edge flap (β).

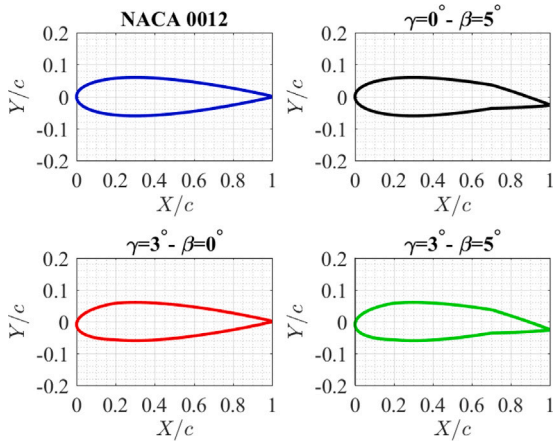

Fig. 3. Reference NACA 0012 profile studied and hydrofoils sections with different flaps.

and tested in the hydrodynamic tunnel at IRENav. The reference one is a symmetrical NACA 0012 and the others have a difference in the flap deflection angles and the rotating position. The different angles involved are described in Fig. 2 α is the angle of incidence, γ is the angle of the leading edge flap and β is the angle of the trailing edge flap.

Fig. 3 shows the four hydrofoil geometries used in this study. One of the hydrofoils has a leading edge flap at 20%c with the deflection angle of $\gamma = 3°$, the second one has a trailing edge flap at 70%c with the deflection angle of $\beta = 5°$ and the last one has the two flaps: leading edge flap at 20%c with the deflection angle of $\gamma = 3°$ and trailing edge flap at 70%c with the deflection angle of $\beta = 5°$. These hydrofoils have the same chord and span as the reference NACA 0012.

Hydrofoils are mounted in the test section using a new system developed in the institute which is named fairing system (support beam). To measure the components of the hydrodynamic forces, hydrofoils are mounted on an axis of rotation at $X/c = 0.25$. The axis of rotation is made of stainless steel to assess the stiffness of the structure of the hydrofoil (Fig. 6). The axis of rotation has a rectangular form and is fastened into the hydrodynamic balance, secured by a tight fitted key/nut system. Then the fairing (Fig. 5) corresponding to the different geometries are slide on the beam (Fig. 4). The beam is

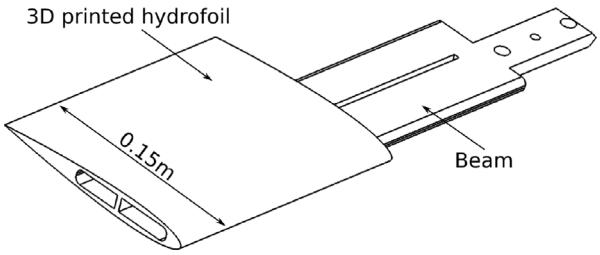

Fig. 4. CAD of NACA 0012 with hydrofoil fairing system.

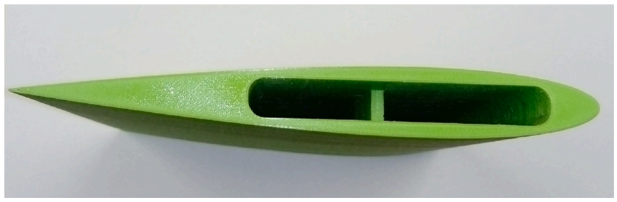

Fig. 5. 3D printing NACA 0012 with fairing system. Chord is 0.15 m.

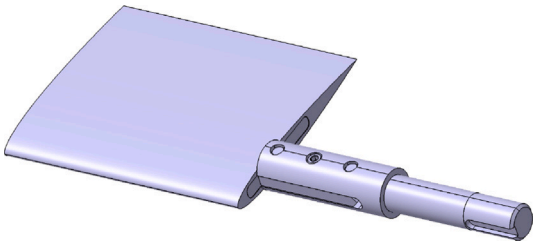

Fig. 6. CAD of NACA 0012 profile with traditional mounting system. Chord is 0.15 m.

mounted to the balance by the mean of a bolted cylinder (Fig. 6). This mounting procedure assure the minimum disturbance of the setting of the hydrodynamic balance.

In the aim to control transition problems, a roughness layer was set on the upper and lower hydrofoils surfaces at 5%c from the leading edge.

2.1. Hydrodynamic balance

Measurement of hydrodynamic forces is performed using a hydrodynamic balance at various conditions of angle of attack. The 5-components hydrodynamic balance has a range up to 1700 N for the lift force, 180 N for the drag and 43 N m for the pitching moment. It is fixed into a supporting frame, mounted on bearings (Fig. 7), and driven in rotation by a Baldor motor. The stepper motor allows for 600 000 impulsions per turn on 360°, meaning a resolution of 0.0006°. The foil is fastened into the balance, secured by a tight fitted key/nut system (Marchand et al., 2017). As the test section is horizontal, the geometric 0° angle of attack of the hydrofoil is visually controlled using the water surface at mid height of the test section when filling the tunnel. Also, as the first hydrofoil is symmetric, the zero-lift angle is used to set the reference angle of attack.

2.2. Cavitation

The cavitation is visually observed under stroboscopic light. The inception condition is determined by increasing the angle of attack at a constant cavitation number until cavitation appeared. It consists in determining the angles and the lift coefficients for which cavitation occurred suction sides for a constant cavitation number. The cavitation inception is considered when an organized spanwise cavitation pattern

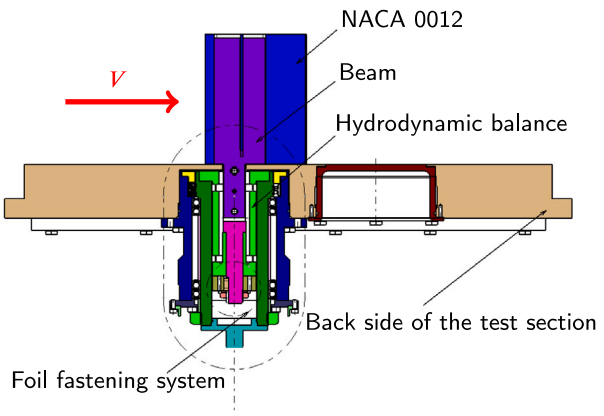

Fig. 7. Overview from top of the mechanical set-up of the hydrodynamic balance.

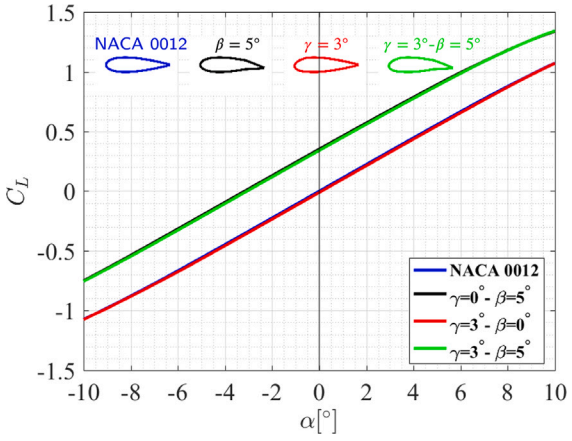

Fig. 8. Effect of the leading edge and trailing edge flaps on the computed lift coefficient evolution as a function of the angle of attack, $Re = 10^6$.

is visually observed along a significant portion of the leading edge. For low cavitation numbers, typically lower than 1.5, the inception angle was determined until the first bubbles were visually detected on the suction side.

This visual technique used in the lab for the best 5 years and have proven not to depend of the user.

2.3. Flow condition and uncertainties

Measurement of hydrodynamic forces is performed using a hydrodynamic balance at various conditions of angle of attack at an inflow velocity of 6.67 m/s corresponding to chord-based Reynolds number of 10^6. Velocity and pressure measurements uncertainties are based on the accuracy of the pressure sensors. The latter is about 0.04 bar. About measurements of hydrodynamic forces and from the document provided by the manufacturer of the hydrodynamic balance, the uncertainties are about ± 1.02 N for the lift, ± 0.324 N for the drag and ± 0.26 N.m for the pitching moment.

3. Numerical approach

The numerical study consists in 2D simulations to investigate the effect of leading and trailing edges deflections on the hydrodynamic performances such as lift, drag and cavitation inception. Cavitation inception prediction is deduced from the $\sigma < -C_{pmin}$ criteria Eq. (1) where C_pmin is determined from subcavitating calculations using Xfoil potential code.

Hydrofoils shapes are plotted using a direct foil design menu of Xfoil, which allows us to define the leading and trailing edges deflections and the rotating flaps positions. After, the flow model of the Xfoil solver is used to evaluate the hydrodynamic performances. The flow model is based on the coupling between a panel method and a boundary layer model used for viscous effect correction. More details about Xfoil are given in Drela (1989). The efficiency of the Xfoil code to predict airfoil performance has been widely endorsed in the literature. Morgado et al. (2016) are conducted a numerical analysis to predict the airfoil aerodynamic performance at low Reynolds numbers using Xfoil code. The results obtained from this analysis are compared to those obtained by using the Shear Stress Transport turbulence model (CFD). At first, they analyzed the influence of the number of points used to define the airfoil inside Xfoil. They concluded that for more than 150 points, Xfoil does not show a significant difference in the airfoil polars. Then, the numerical aerodynamic coefficients obtained from Xfoil code and CFD simulations were compared to the experimental ones presented by Selig et al. in Selig and Guglielmo (1997). It has been shown that the aerodynamic coefficients calculated by Xfoil code are of the same order of magnitude as those obtained from the CFD simulations (ANSYS Fluent and OpenFoam) and the experimental results presented in Selig and Guglielmo (1997). It was concluded the way that Xfoil code predicts the airfoil performance is as good as any of the other used methods.

The efficiency of Xfoil code results were also analyzed by Gunel et al. (2016). They compared the aerodynamic performance calculated by using Xfoil code and transition $SSTk-\omega$ model at low Reynolds number. They observed that the CFD results and Xfoil code results were compatible with each other until stall angle.

Potential and viscous flow predictions are rather close to each other at high Reynolds numbers when considering turbulent flows and laminar to turbulent transition as modeled in Xfoil calculations Xfoil's transition model has been compared to other methods by Holman and Fürst (2021). The Xfoil code has been widely used to predict cavitation inception based on subcavitating minimum pressure coefficient value in many hydrodynamic applications such as marine propellers, hydraulic turbines or marine current turbines. Pan (2011) mentioned several works which highlighted the good agreement between BEM/Xfoil model predictions, RANSE simulations and experimental data concerning pressure distributions and cavitation inception for the fully wetted case (Brewer and Kinnas, 1997, Singh, 2009). Ladino (2011) used Xfoil to predict hydrofoils cavitation buckets and Roca Conesa and Liem (Conesa and Liem, 2018) conducted a multiparametric study to determine the more suitable hydrofoil when considering cavitation inception conditions prediction based on minimum local pressure coefficient value. Cavitation models based on constant water vapor pressure imposed on the cavity surface streamline are not used in our study.

The panel method speeds-up flow calculations as compared to finite volume method. Calculations are carried out using 200 points mesh sizes issued from mesh sensitivity analysis.

Simulations are carried out for a Reynolds number of 10^6 and different angles of attack.

4. Results and discussion

4.1. Numerical results

The effect of the leading and trailing edges deflection angles is predicted using Xfoil software. Fig. 8 illustrates the numerical lift coefficients of the different hydrofoils. As expected the trailing edge flap increases the lift coefficient of the hydrofoil. At the opposite, the leading edge deflection angle has very little effect on the lift coefficient. For the same angle of attack, the trailing edge flap increases the lift coefficient of about $\Delta C_L = 0.35$. When, the same operating point $C_L = 0.5$ is considered, the trailing edge $\beta = 5°$ decreases the angle

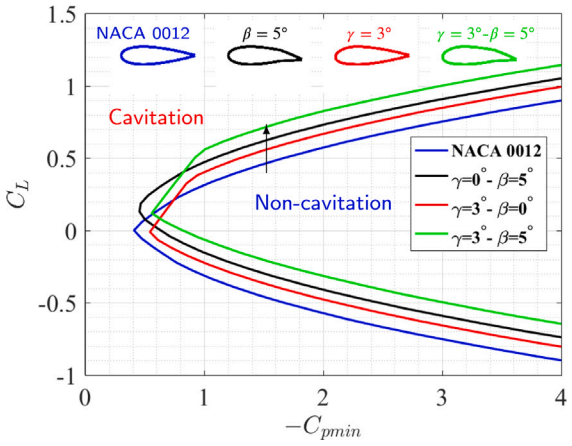

Fig. 9. Numerical cavitation bucket of NACA 0012, NACA 0012 with leading edge flap, NACA 0012 with trailing edge flap and NACA 0012 with leading and trailing edge flaps, $Re = 10^6$.

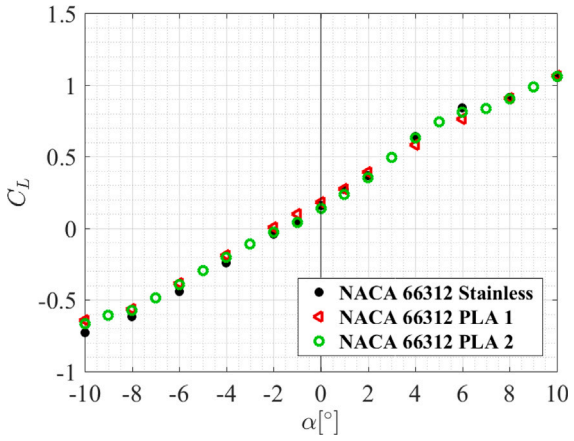

Fig. 10. Experimental lift coefficients of both NACA 66312 hydrofoil made of stainless steel and PLA, $Re = 5.33\ 10^5$.

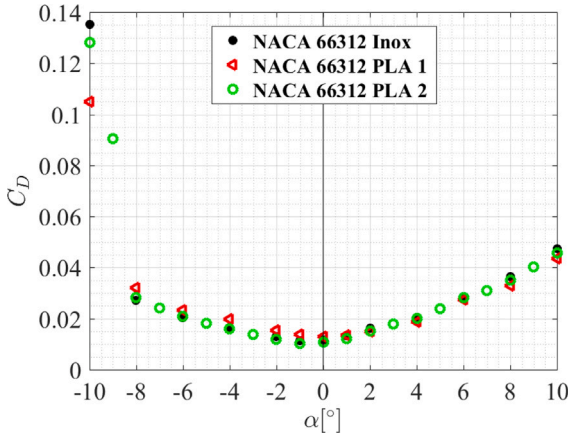

Fig. 11. Experimental drag coefficients of both NACA 66312 hydrofoil made of stainless steel and PLA, $Re = 5.33\ 10^5$.

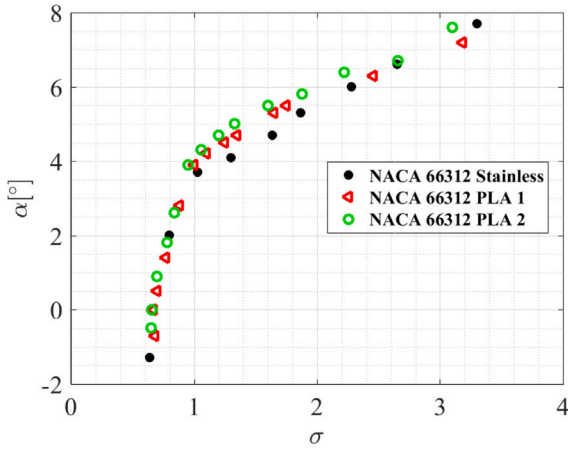

Fig. 12. Experimental cavitation buckets of NACA 66312 profiles made of stainless steel and of PLA, $Re = 5.33\ 10^5$.

of attack from 4.48° to 1.35° ($\Delta\alpha = 3.13°$). Results are consistent with the hydrodynamic co tendencies.

The effect of the flaps deflections on the cavitation inception is also predicted using Xfoil analysis using the criteria ($-C_{pmin} = \sigma$). Fig. 9 shows the lift coefficient versus the opposite of the minimum pressure coefficient ($-C_{pmin}$) of the four hydrofoils.

Flaps deflection has a direct influence on the theoretical cavitation inception, particularly for lift coefficients larger than 0.075. It is found that the leading and trailing edges deflections enlarge the non-cavitation domain. It is shown that the flap deflection makes the cavitation bucket to shift up. For low lift coefficients, the trailing edge flap is sufficient to delay the cavitation inception. For the high lift coefficients, the leading edge flap is necessary to enlarge the non-cavitation domain and it provides a significant gain.

4.2. Experimental validation of the fairing system

In this work, we study the use of fast and inexpensive additive building process for experimental cavitation study in hydrodynamic tunnel. Two fairings 3D printed in PLA are then compared to a machine cut Stainless foil to check the accuracy and repeatability of the 3D printing process and the fairing concept Fig. 4. Hydrodynamic coefficients measured on the PLA-NACA 66312 hydrofoils mounted using a fairing system are compared to those measured on the stainless steel NACA 66312 hydrofoil mounted using the traditional mounting system. This type of profile is often used for the propeller blades in industry and widely studied at IRENav (Leroux et al., 2005; Ducoin, 2008).

The experimental evolution of the lift and drag coefficients as a function of the angle of attack are presented respectively in Figs. 10 and 11. They summarize the experimental coefficients measured on the hydrofoil made of stainless steel and on the hydrofoils faring manufactured using 3D printer technique.

It is shown that the lift coefficient measured on the stainless steel profile has the same trend as the one measured on hydrofoils manufactured in 3D printing. The same remark is obtained for the drag coefficient. During this analysis, the maximum difference between the experimental lift coefficients is about 0.087. This difference was noted at $\alpha = -10°$ angle of incidence between the stainless steel profile and the PLA 1 profile. For the drag coefficient, the maximum difference is obtained for the same angle of incidence ($\alpha = -10°$) where stall occurs and causes important fluctuation in the drag, impacting the measurement. Far from the stall area, the maximum difference between the C_L measured on the hydrofoils made of the stainless steel and PLA 1 is about 0.076 noted at $\alpha = 6°$.

The cavitation inception on the NACA 66312 hydrofoils made using 3D printer technique is compared to the cavitation inception obtained on the same type of hydrofoil made of stainless steel. Various measurement campaigns were carried out at $5.33\ 10^5$ Reynolds number. The experimental cavitation buckets are presented in Fig. 12.

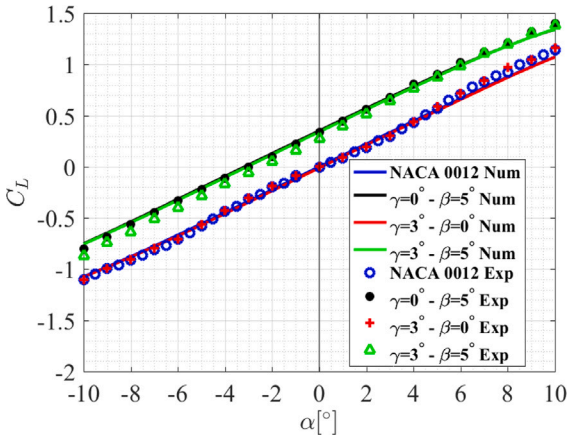

Fig. 13. Experimental and numerical lift coefficients of the four hydrofoils, $Re = 10^6$.

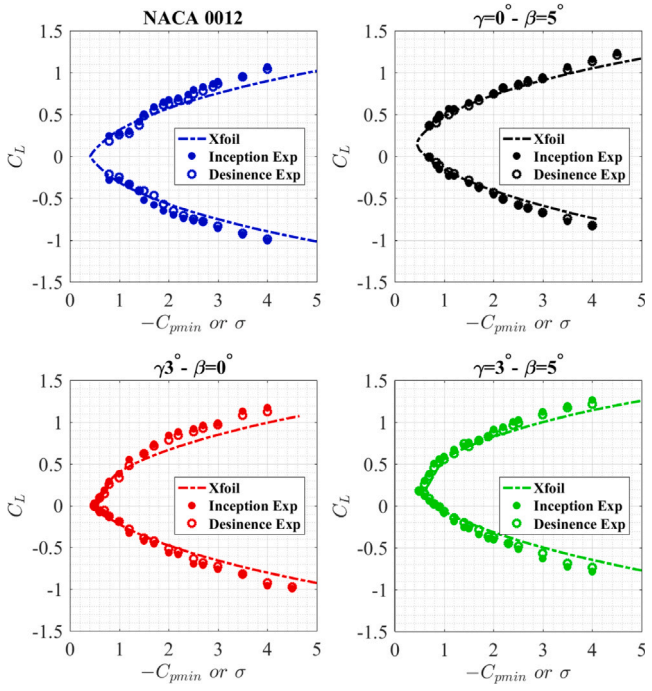

Fig. 14. Experimental cavitation inception and desinence compared to the numerical ones of the NACA 0012 and hydrofoils with flaps, $Re = 10^6$.

The conditions of cavitation inception on the PLA hydrofoils suction side are similar to those of cavitation inception on the stainless steel hydrofoil. However, the values are lower for the stainless steel hydrofoil. The order of maximum difference between the angles of the cavitation inception on the stainless steel hydrofoil and the hydrofoil made of PLA is about $\Delta\alpha = 0.8°$ noted at the cavitation numbers $\sigma = 1.6$ and $\sigma = 1.3$. Discrepancies can be explained by different reason from the difference of step of incidence $\Delta\alpha$ chosen, the fluctuations of speed and pressure in the test section and the speed control setting due to blockage effect. We conclude that the 3D printed faring can be used for cavitation experimental campaign.

4.3. Experimental results of the effect of flap on hydrodynamic performances

The 3D printed hydrofoils are studied in cavitation tunnel at IRENav. For a Reynolds number $Re = 10^6$, the lift coefficients measured using the hydrodynamic balance are presented in Fig. 13. These

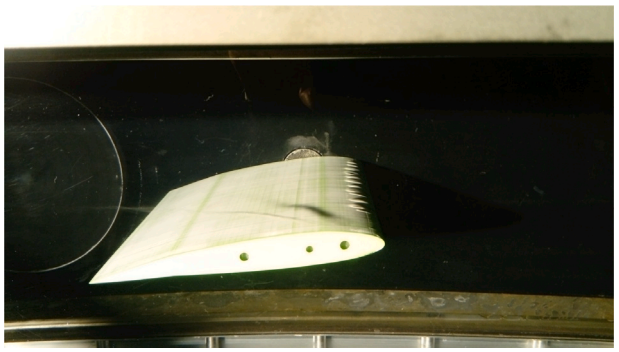

Fig. 15. Experimental cavitation inception on the hydrofoil surface, $Re = 10^6$, PLA 3D printed fairing hydrofoils, $\gamma = 3°$, $\beta = 5°$.

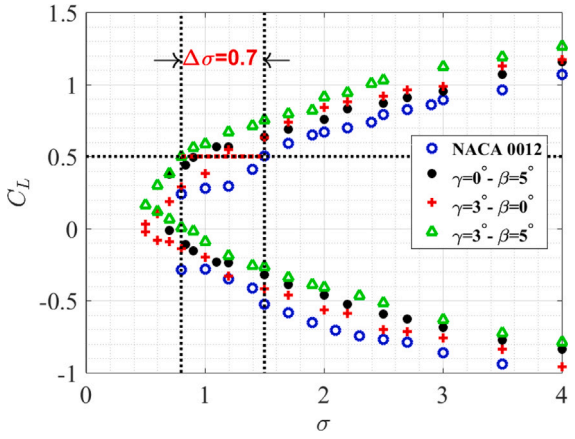

Fig. 16. Effet of the flaps on the experimental cavitation buckets of the NACA 0012.

experimental results are compared to the numerical ones obtained from the numerical study. The experimental results for the four hydrofoils fit with the numerical ones showing the ability of Xfoil to simulate the hydrodynamic performance. Fig. 13 presents the experimental and numerical lift coefficients of the four hydrofoils.

For each hydrofoil and various cavitation numbers, cavitation inception and desinence are investigated. They are compared to the theoretical bucket predicted using Xfoil as presented in Fig. 14 which summarizes the conditions for cavitation inception and desinence on the hydrofoils surfaces. The abscissa denotes the cavitation number when the ordinate denotes the lift coefficient for which cavitation is visually detectable. A good agreement is found between numerical and experimental results, particularly for low lift coefficients and cavitation desinence. For $C_L > 0.6$ the experimental cavitation bucket discard from the numerical ones. An hysteresis between the cavitation inception and desinence for the same cavitation number is observed. This hysteresis means that the pressure required for the cavitation inception must be less than the pressure required for the cavitation desinence (Astolfi et al., 2000). Fig. 15 illustrates the observed cavitation, located at the leading edge, on a 3D printed hydrofoil.

To highlight the effect of leading and trailing edge flaps, the variation of cavitation number for the same operating point is extracted. For the same lift coefficient $C_L = 0.5$, the non-cavitation domains enlarged from about $\Delta\sigma = 0.7$ (Fig. 16).

This enlargement of the non-cavitation domain is well predicted by the numerical model.

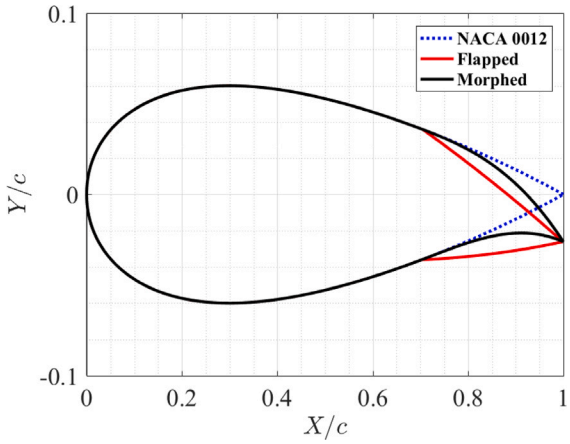

Fig. 17. The geometries of the symmetrical hydrofoil and the hydrofoils with the traditional and parabolic flaps, $\beta = 5°$.

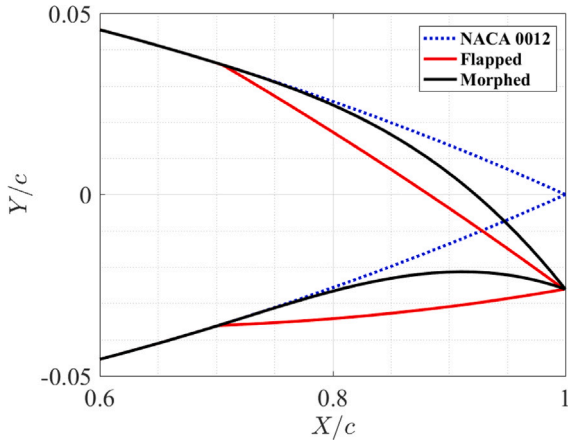

Fig. 18. The geometries of the trailing edges of the symmetrical hydrofoil and the traditional and parabolic flaps, $\beta = 5°$.

4.4. *Effect of the trailing edge flap shape on the hydrodynamic performance*

In aerodynamics, several studies have been carried out in order to define the shape of the trailing edge flap which allows the same deflection as the traditional flap, but which eliminates the discontinuities in the pressure coefficient distribution. To define the camber line of the morphing trailing edge, Abdessemed et al. (2017) used a third order polynomial that is given by the Eq. (3) and they compared the results of the morphed airfoil to those of a flapped airfoil. It was observed that the morphed airfoil produced a higher lift/drag ratio than the flapped one.

The same equation for the camber line of the trailing edge flap was used by Hunsaker et al. (2019). The objective is to suppress the discontinuous camber line slope at the hinge point of the traditional flap. They have shown that the contribution of this type of flap can be 33 to 50% more than that of the traditional flap.

The Eq. (3) represents the third order polynomial which defines the camber line of the morphing part of the hydrofoil (flap). This equation is added to the equation of the thickness distribution of a four-digit NACA profile which is defined in Eq. (4).

$$Y_c = \begin{cases} 0, 0 \le X \le X_s \\ -w_{te}\dfrac{(X - X_s)^3}{(1 - X_s)^3}, X \ge 0 \end{cases} \tag{3}$$

With Y_c is the camber line of the morphing part of the hydrofoil, X is the non-dimensional chord, X_s chordwise start location of morphing, w_{te} is the value of maximum deflection at the trailing edge.

$$Y_t = (th/c)\begin{pmatrix} 0.2969\sqrt{X} - 0.1260X - 0.3516X^2 \\ +0.2843X^3 - 0.1510X^4 \end{pmatrix} \tag{4}$$

Y_t is the hydrofoil thickness distribution and th is the non-dimensional hydrofoil thickness ($th = 0.12$ for NACA 0012).

Fig. 17 represents the geometry of the symmetrical hydrofoil (NACA 0012), the geometry of the hydrofoil with the morphed trailing edge flap defined by a third order polynomial (Eq. (3)) and the geometry of the NACA 0012 hydrofoil with a traditional flap. In this study, the deflection of the two flaps is about 5° and the hinge point or the rotation axis of the flap is located at 70% of the chord. The shapes of the trailing edge flaps are shown in Fig. 18. The latter shows that the flap with a parabolic shape eliminates the discontinuity at the hinge point, assuring therefore a better surface continuity condition.

The different hydrofoils presented previously are numerically analyzed using Xfoil at the same flow conditions ($Re = 10^6$, $N_{crit} = 9$, $Xtr = 0.05$ and $-10° < \alpha < +10°$). The lift coefficients are presented in Fig. 19. At $\alpha = 0°$, the traditional flap at 5° allows the increase of the

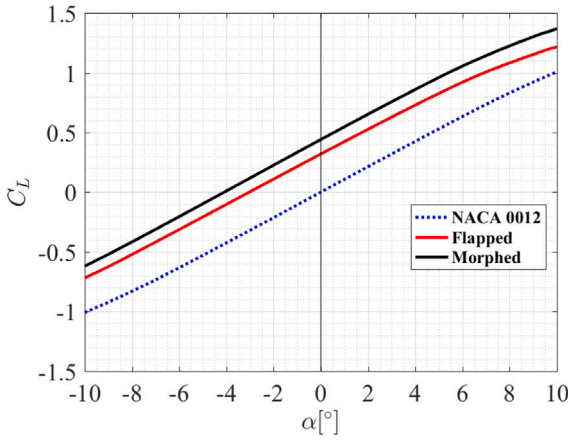

Fig. 19. Lift coefficients as a function of the angle of incidence of the NACA 0012 hydrofoil, the hydrofoil with a traditional trailing edge flap at 5° and the hydrofoil with a parabolic trailing edge flap, $Re = 10^6$.

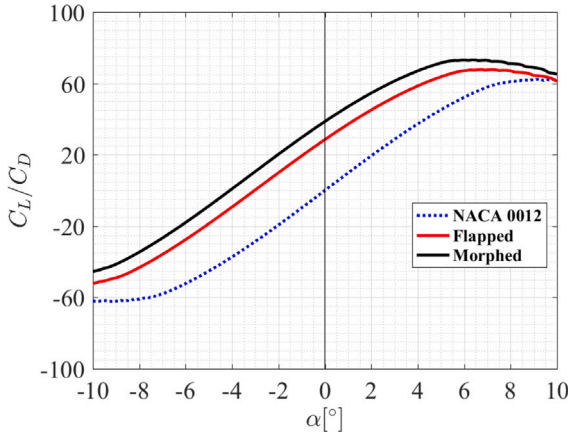

Fig. 20. C_L/C_D as a function of the angle of incidence of the NACA 0012 hydrofoil, the hydrofoil with a traditional trailing edge flap at 5° and the hydrofoil with a parabolic trailing edge flap, $Re = 10^6$.

C_L about 0.329, but the parabolic flap allows a better increase of the lift coefficient. The last one is about 0.45 compared to the hydrofoil without flap and it is about 0.12 when it is compared to the hydrofoil with the traditional flap at the same trailing edge deflection angle.

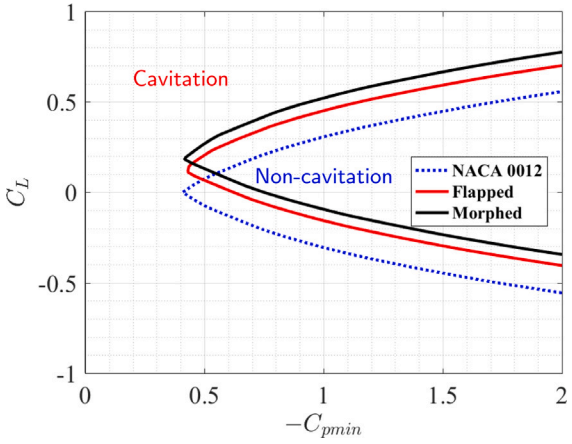

Fig. 21. Predicted cavitation buckets of the hydrofoil without flap, hydrofoil with a traditional trailing edge flap at 5° and the hydrofoil with a parabolic trailing edge flap, $Re = 10^6$, $N_{crit} = 9$ and $Xtr = 0.05$.

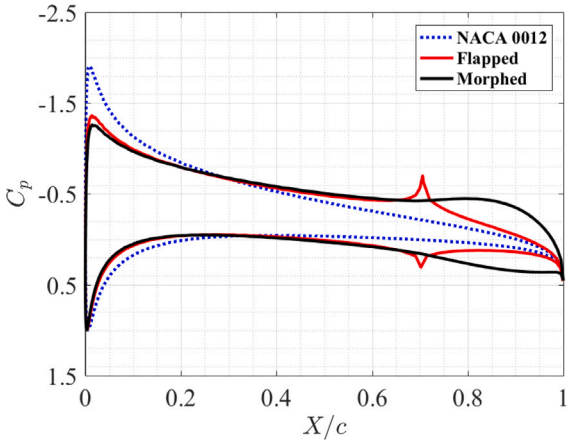

Fig. 22. Pressure coefficient distribution calculated along the surface of the NACA 0012 without flap, with the traditional trailing edge flap and with the parabolic trailing edge flap at $C_L = 0.5$, $\beta = 5°$, $Re = 10^6$, $N_{crit} = 9$ and $Xtr = 0.05$.

The trailing edge flaps have also an advantage on the C_L/C_D ratios of the initial hydrofoil. The effects of the traditional and parabolic trailing edge flaps on the C_L/C_D ratios are presented in Fig. 20. It is observed that the C_L/C_D of the hydrofoil with the parabolic trailing edge flap is higher than the C_L/C_D of the hydrofoil with the traditional flap.

In this part, the effect of the trailing edge flap shape on the cavitation bucket of the initial hydrofoil (NACA 0012) is analyzed. The lift coefficient versus the opposite of the minimum pressure coefficient ($-C_{pmin}$) for the three hydrofoils are presented in Fig. 21. It is shown that the traditional flap enlarges the non-cavitation domain for $C_L >$ 0.067 and the parabolic flap for $C_L > 0.107$. For a lift coefficient greater than 0.16, the morphed flap shits up the cavitation bucket with no significant effect on the area of the bucket itself. For an operating point characterized by a $C_L = 0.5$, the hydrofoil with a traditional trailing edge flap decreases the cavitation number about 0.581 as it is compared to the cavitation number of the hydrofoil without flap. The gain at $C_L = 0.5$ of the parabolic flap on cavitation number is $\Delta\sigma = 0.213$ of the flapped hydrofoil, representing a total gain of 0.794 with the NACA 0012.

At the operating point $C_L = 0.5$ and the same flow conditions ($Re = 10^6$, $N_{crit} = 9$ and $Xtr = 0.05$), the pressure coefficient distributions around the three hydrofoils are plotted in Fig. 22. A pressure spike at the hinge point is caused by the discontinuity in the camber line

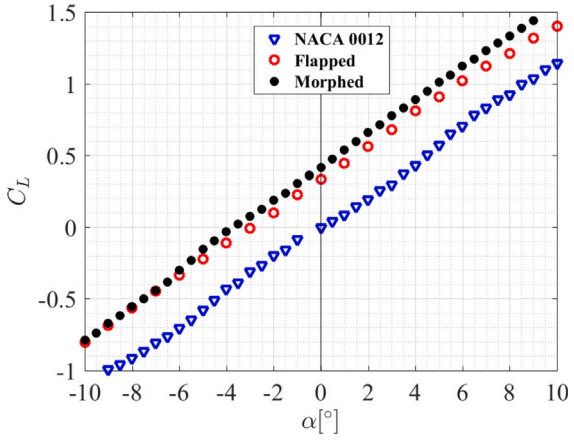

Fig. 23. Lift coefficient experimentally measured on the NACA 0012 without flap, with the traditional trailing edge flap and with the parabolic trailing edge flap, $Re = 10^6$.

slope of the traditional flap. This large pressure gradient can induce flow separation at the hinge point. The parabolic flap suppresses the pressure spike at the hinge point, but enlarges the pressure gradient near the hydrofoil trailing edge, which can induce flow separation in this region.

In the last part, we experimentally compared the results of the morphing trailing edge by manufacturing a hydrofoil with a parabolic flap using a 3D printer technique. The experiments are carried out in the hydrodynamic tunnel at the IRENav with an inflow condition of $Re = 10^6$ and different angles of attack. The lift and drag coefficients are measured using the hydrodynamic balance. Results are compared to the hydrofoil with a traditional flap at 5°.

Fig. 23 shows the experimental lift coefficients measured on the symmetrical hydrofoil (NACA 0012), the hydrofoil with a traditional flap ($\beta = 5°$) and the hydrofoil with a parabolic trailing edge flap (Eq. (3)). These experiments highlight the effect of the trailing edge flap on the lift coefficient of the hydrofoil without flap. From the Fig. 23, it is clearly shown that the flap camber significantly increases the lift coefficient of the hydrofoil at the studied conditions.

It is noted that for the same deflection angle ($\beta = 5°$), the parabolic trailing edge flap produces a higher lift coefficient with an increase in the lift coefficient of about 11% at $\alpha = 5°$ as compared with the C_L of the flapped hydrofoil.

Fig. 24 illustrates the experimental lift-to-drag ratio. The morphed and the flapped hydrofoils have their maximum C_L/C_D shifted to the left due to the flap. At low C_L (α −10° to 0°) the morphed has a better performance than the flapped when the inverse tendency is observed at high lift. The morphed hydrofoil has a clear advantage on drag at low C_L.

Fig. 25 summarizes the cavitation buckets of the symmetrical hydrofoil, flapped and morphed hydrofoils. These results confirm the behavior that was predicted previously using Xfoil. The cavitation bucket moves up for the hydrofoils with trailing edge flaps. The flapped and the morphing trailing edges enlarge the non-cavitation domain of the initial hydrofoil for the positive lift coefficient. The hydrofoil with a parabolic trailing edge flap pushes the cavitation further away than the hydrofoil with a traditional flap. For example, at $C_L = 0.5$, the morphed hydrofoil gives a variation of cavitation number of 0.34 as compared to the flapped hydrofoil.

5. Leading and trailing edge flaps effect on the hydrodynamic performance

From the study presented in the previous sections, it has been shown that the hydrodynamic performance predicted using Xfoil software are

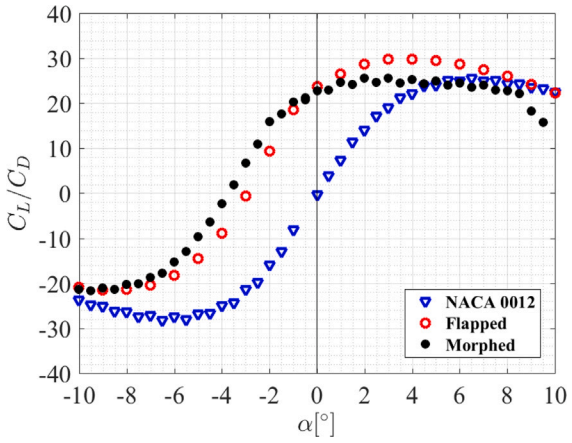

Fig. 24. Experimental hydrodynamic lift to drag ratio versus angle of attack for initial hydrofoil and hydrofoils with morphed and flapped trailing edges, $Re = 10^6$, $\beta = 5°$.

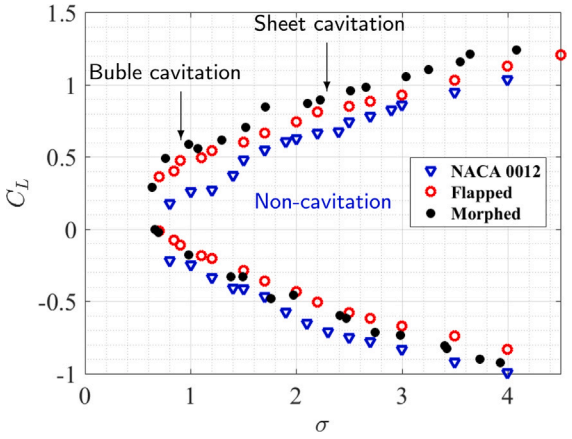

Fig. 25. Experimental cavitation buckets of the NACA 0012 without flap, with the traditional trailing edge flap and with the parabolic trailing edge flap, $Re = 10^6$.

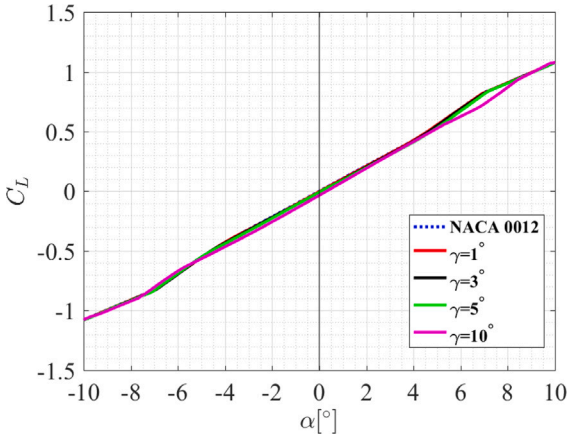

Fig. 26. Numerical lift coefficient as a function of angle of attack and leading edge deflection angle, $Re = 10^6$.

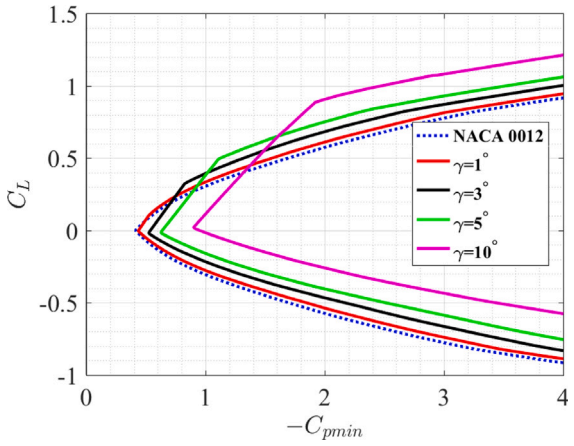

Fig. 27. Numerical cavitation bucket for NACA 0012 without and with different leading edge flap angles, $Re = 10^6$.

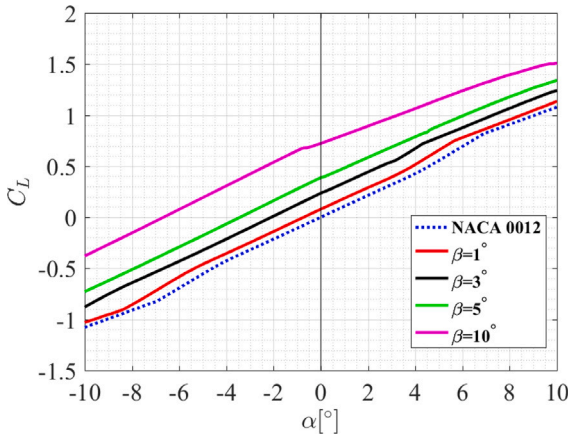

Fig. 28. Numerical lift coefficient as a function of angle of attack and trailing edge deflection angle, $Re = 10^6$.

in good agreement with the experimental measurements. To complete this study and to understand the evolution of the hydronamic performance as a function of variation in foil characteristics, the effect of the leading and the trailing edge flaps is studied individually.

5.1. Leading edge flap angle effect on the hydrodynamic performance

Simulations are conducted with Xfoil for $Re = 10^6$ and four LE flap angles ($\gamma = 1°$, $\gamma = 3°$, $\gamma = 5°$ and $\gamma = 10°$) and the axis of rotation of the flaps is positioned at $X/c = 20\%c$. Figs. 26 and 27 present the lift coefficient as a function of angle of attack and the cavitation bucket as function of the leading edge deflection angle respectively. It is shown that the leading edge deflection has not a significant effect on the lift coefficient, but an effect on the cavitation bucket. The increase of the leading edge deflection moves The cavitation bucket slides up with the leading edge flap angle. The cavitation domain is increased at low C_L, the bucket being indeed truncated and taking a sharp shape.

5.2. Trailing edge flap angle effect on the hydrodynamic performance

Simulations are conducted with Xfoil at $Re = 10^6$ and four trailing edge deflection angles ($\beta = 1°$, $\beta = 3°$, $\beta = 5°$ and $\beta = 10°$) and the axis of rotation of the flaps is positioned at $X/c = 70\%c$. As expected, the trailing edge deflection has an important effect on the lift coefficient as observed in Fig. 28, adding camber to the foil. If the evolution of C_L reminds parallel at small LE flap angles, the slope $C_L(\alpha)$ decreases

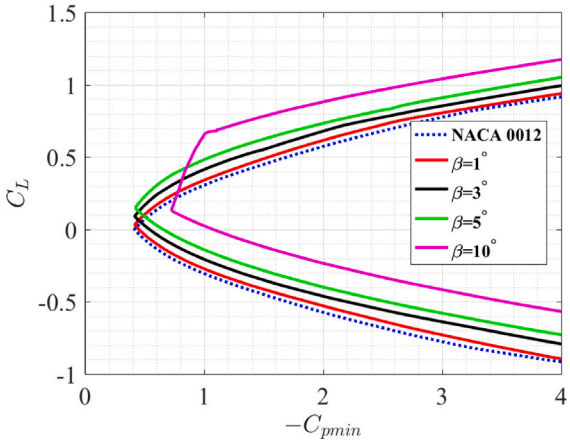

Fig. 29. Numerical cavitation bucket for NACA 0012 without and with trailing edge flaps, $Re = 10^6$.

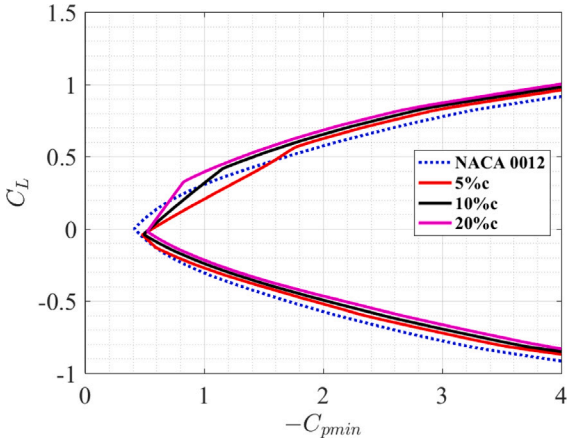

Fig. 30. Numerical cavitation bucket for NACA 0012 without and with leading edge flaps at $\gamma = 3°$ and different flap position, $Re = 10^6$.

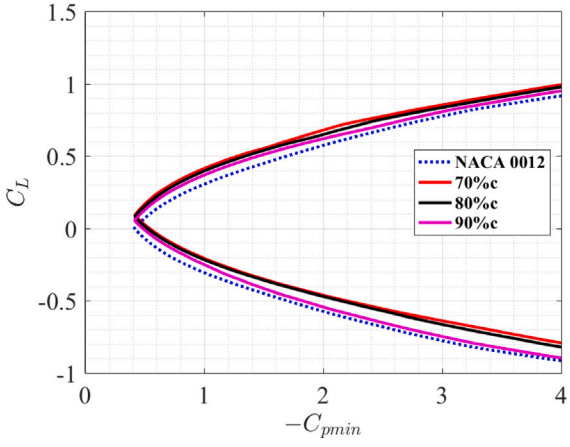

Fig. 31. Numerical cavitation bucket for NACA 0012 without and with trailing edge flaps at $\beta = 3°$ and different flap position, $Re = 10^6$.

significantly at positive angle of attack. The lift gain with TE flap has the only effect to slides up the cavitation bucket at low angles ($\leq 5°$) when the cavitation domain increases at low C_L at $\beta = 10°$ Fig. 29.

5.3. Flap position effect on the hydrodynamic performance

The effect of the position of the LE and TE deflections on the lift coefficient and cavitation envelope is studied at $Re = 10^6$ and the results are presented in Figs. 30 and 31. The position of the leading edge deflection has a small effect on the cavitation bucket, impacting the low C_L domain. The cavitation domain increases when the flap's hinge moves backward. For the TE deflection, the position ogf the flap has not a great impact on the cavitation domain but is small increased at $C_L < 0$ when the rotation point is at the really back of the foil ($X/c = 90\%$). At ($X/c = 90\%$), the effect of the lift is then minimized (see Fig. 28).

6. Conclusions

In this paper, an experimental and a numerical study have been presented in order to assess the effect of the leading and trailing edge flaps on the hydrodynamic performances of a hydrofoil. Fast additive 3D printing process using PLA is used to generate the foils envelopes.

Firstly, the effect of the leading and trailing edge flaps deflection angles on the hydrodynamic coefficients and cavitation bucket is analyzed at $Re = 10^6$ using Xfoil software. Then, the effect of the trailing edge flap shape on the hydrodynamic performance is studied. The hydrodynamic coefficients of a hydrofoil with a traditional trailing edge flap at $\beta = 5°$ are compared to the same hydrofoil with a parabolic trailing edge flap.

Experimentally, four hydrofoils are manufactured using 3D printing technique and tested in the hydrodynamic tunnel at IRENav. The first hydrofoil is the reference NACA 0012 without flaps, the second hydrofoil has a trailing edge flap of $\beta = 5°$ at $70\%c$, the third one has a leading edge flap of $\gamma = 3°$ at $20\%c$ and the hydrofoil has a leading and trailing edge flaps of $\gamma = 3°$ and $\beta = 5°$ respectively. Hydrodynamic forces are measured using the hydrodynamic balance. To analyze the cavitation inception, the experimental cavitation buckets are plotted for the different hydrofoils and compared to the theoretical ones predicted by Xfoil model base on the $-C_{pmin}$ criteria. The PLA 3D printed foils have proved to be a fast, unexpensive and reliable technology for cavitation studies.

Xfoil simulations show that the trailing edge deflection angle increases the lift coefficient, contrary to the leading edge which has not an effect on the hydrodynamic forces. It is also noted that the leading and trailing edge deflections slides up the cavitation bucket and tends to decrease the non-cavitation domain of hydrofoil NACA 0012. Results of these simulations are compared to the experimental ones obtained in the cavitation tunnel at IRENav. It is concluded that the numerical fit well the experimental ones.

The shape of the trailing edge flap affects the hydrodynamic coefficients and the cavitation bucket. The hydrofoil with a parabolic flap gives more lift that the traditional flap and can enlarge the non-cavitation domain to some extent of the lift coefficients. This study also shows that the parabolic trailing edge flap suppresses the pressure spike at the hinge point caused by the traditional trailing edge flap. The results of these simulations are confirmed by the experimental test.

Eventually, a numerical study of the effect of trailing and leading edge flaps allows to extend the conclusion and confirm the observed tendencies which are a shift up and decrease of the non-cavitation domain with the increase of the deflection angle.

Nomenclature

α	angle of attack [°].
β	trailing edge deflection [°].
γ	leading edge deflection [°].
ρ	fluid density [kg/m^3].
σ	cavitation number: $\sigma = \frac{P-P_v}{\frac{1}{2}\rho V^2}$ [–].
c	hydrofoil chord [m].
C_D	drag coefficient: $C_D = \frac{D}{\frac{1}{2}\rho V^2 s}$ [–].
C_L	lift coefficient: $C_L = \frac{L}{\frac{1}{2}\rho V^2 s}$ [–].
C_p	pressure coefficient: $C_p = \frac{P-P_{ref}}{\frac{1}{2}\rho V^2}$ [–].
D	drag force [N].
e	hydrofoil span [m].
h	immersion of the hydrofoil [m].
L	lift force [N].
P	pressure [bar].
Re	Reynolds number: $Re = Vc/\nu$ [–].
s	hydrofoil planform [m^2].
V	inflow velocity [m/s].
X, Y, Z	foil coordinates [m].
ν	kinematic viscosity [m^2/s].

Acknowledgments

The authors would like to thank the technical staff of the French Naval Academy Research Institute for their support to this study.

References

Abdessemed, C., Yao, Y., Narayan, P., Bouferrouk, A., 2017. Unsteady parametrization of a morphing wing design for improved aerodynamic performance. 3AF International Conference on Applied Aerodynamics March 2017.

Arab, F.M., Augier, B., Deniset, F., Casari, P., Astolfi, J.A., 2019. Morphing hydrofoil model driven by compliant composite structure and internal pressure. J. Mar. Sci. Eng. 7 (12), 423.

Astolfi, J.-A., Dorange, P., Billard, J.-Y., Tomas, I.C., 2000. An experimental investigation of cavitation inception and development on a two-dimensional eppler hydrofoil. J. Fluids Eng. 122 (1), 164–173.

Barbarino, S., Bilgen, O., Ajaj, R.M., Friswell, M.I., Inman, D.J., 2011. A review of morphing aircraft. J. Intell. Mater. Syst. Struct. 22 (9), 823–877.

Brailovski, V., Terriault, P., Coutu, D., Georges, T., Morellon, E., Fischer, C., Bérubé, S.b., 2008. Morphing laminar wing with flexible extrados powered by shape memory alloy actuators. In: Smart Materials, Adaptive Structures and Intelligent Systems, Vol. 43314. pp. 615–623.

Brewer, W.H., Kinnas, S.A., 1997. Experiment and viscous flow analysis on a partially cavitating hydrofoil. J. Ship Res. 41 (03), 161–171.

Conesa, F.R., Liem, R.P., 2018. Numerical investigation of cavitation performance of slotted hydrofoil for amphibious aircraft. The 2018 Structures Congress,Songdo Convensia, Incheon, Korea 124.

Drela, M., 1989. Xfoil: An analysis and design system for low Reynolds number airfoils. In: Low Reynolds Number Aerodynamics. Springer, pp. 1–12.

Ducoin, A., 2008. Etude Expérimentale Et Numérique Du Chargement Hydrodynamique Des Corps Portants En Régime Transitoire Avec Prise En Compte Du Couplage Fluide Structure (Ph.D. thesis). Nantes.

Ducoin, A., Astolfi, J.A., Sigrist, J.F., 2012. An experimental analysis of fluid structure interaction on a flexible hydrofoil in various flow regimes including cavitating flow. Eur. J. Mech. B Fluids 63–74.

Gaggero, S., Gonzalez-Adalid, J., Sobrino, M.P., 2016. Design of contracted and tip loaded propellers by using boundary element methods and optimization algorithms. Appl. Ocean Res. 55, 102–129.

Garg, N., Kenway, G., Martins, J., Young, Y., 2016. High-fidelity hydrostructural optimization of a 3-D hydrofoil. In: International Symposium on Transport Phenomena and Dynamics of Rotating Machinery, Honolulu, HI, Apr. pp. 10–15.

Garg, N., Kenway, G.K., Martins, J.R., Young, Y.L., 2017. High-fidelity multipoint hydrostructural optimization of a 3-d hydrofoil. J. Fluids Struct. 71, 15–39.

Garg, N., Lyu, Z., Dhert, T., Martins, J., Young, Y.L., 2015. High-fidelity hydrodynamic shape optimization of a 3-d morphing hydrofoil. In: Fourth International Symposium on Marine Propulsors.

Garg, N., Pearce, B.W., Brandner, P.A., Phillips, A.W., Martins, J.R., Young, Y.L., 2019. Experimental investigation of a hydrofoil designed via hydrostructural optimization. J. Fluids Struct. 84, 243–262.

Giovannetti, L.M., Banks, J., Ledri, M., Turnock, S.R., Boyd, S.W., 2018. Toward the development of a hydrofoil tailored to passively reduce its lift response to fluid load. Ocean Eng. 167 (1), 1–10.

Gunel, O., Koç, E., Yavuz, T., 2016. Comparison of CFD and xfoil airfoil analyses for low Reynolds number. Int. J. Energy Appl. Technol. 3 (2), 83–86.

Guo, S., 2020. Morphing wing technologies: large commercial aircraft and civil helicopters. The Aeronautical Journal 124 (1282), 2048–2053.

Holman, J., Fürst, J., 2021. Numerical simulation of separation induced laminar to turbulent transition over an airfoil. J. Comput. Appl. Math. 394, 113530.

Hunsaker, D.F., Reid, J.T., Joo, J.J., 2019. Geometric definition and ideal aerodynamic performance of parabolic trailing-edge flaps. Int. J. Astronaut. Aeronaut. Eng. 4.

Jawahar, H.K., Ai, Q., Azarpeyvand, M., 2018. Experimental and numerical investigation of aerodynamic performance for airfoils with morphed trailing edges. Renew. Energy 127, 355–367.

Kaul, U.K., Nguyen, N.T., 2018. Drag characterization study of variable camber continuous trailing edge flap. J. Fluids Eng. 140 (10), 101108.

Kawanami, Y., Kato, H., Yamaguchi, H., Tanimura, M., Tagaya, Y., 1997. Mechanism and control of cloud cavitation. J. Fluids Eng. 119 (4), 788–794.

Ladino, A., 2011. Numerical study of cavitation characteristics of profiles for use in marine current turbines. In: ASME International Mechanical Engineering Congress and Exposition. Vol. 54877. pp. 863–868.

Lelong, A., Guiffant, P., Astolfi, J.A., 2016. An experimental analysis of the structural response of flexible lightweight hydrofoils in various flow conditions. In: 16th International Symposium on Transport Phenomena and Dynamics of Rotating Machinery.

Lelong, A., Guiffant, P., Astolfi, J.A., 2018. An experimental analysis of the structural response of flexible lightweight hydrofoils in cavitating flow. J. Fluids Eng. 140 (2), 021116.

Leroux, J.-B., Coutier-Delgosha, O., Astolfi, J.A., 2005. A joint experimental and numerical study of mechanisms associated to instability of partial cavitation on two-dimensional hydrofoil. Phys. Fluids 17 (5), 052101.

Marchand, J.B., Astolfi, J.A., Bot, P., 2017. Discontinuity of lift on a hydrofoil in reversed flow for tidal turbine application. Eur. J. Mech. B Fluids 63, 90–99.

Morgado, J., Vizinho, R., Silvestre, M., Páscoa, J., 2016. XFOIL vs CFD performance predictions for high lift low Reynolds number airfoils. Aerosp. Sci. Technol. 52, 207–214.

Pan, Y., 2011. A viscous/inviscid interactive approach for the prediction of performance of hydrofoils and propellers with nonzero trailing edge thickness. J. Ship Res. 55 (01), 45–63.

Sacher, M., Durand, M., Berrini, E., Hauville, F., Duvigneau, R., Le Maitre, O., Astolfi, J.A., 2018. Flexible hydrofoil optimization for the 35th America's cup with constrained EGO method. Ocean Eng. 157, 62–72.

Selig, M.S., Guglielmo, J.J., 1997. High-lift low Reynolds number airfoil design. J. Aircr. 34 (1), 72–79.

Singh, S., 2009. Viscous/inviscid flow around 2-D and 3-D hydrofoils with emphasis on leading edge flow separation. (Ph.D. thesis). University of Texas at Austin.

Sun, Z., Mao, Y., Fan, M., 2020. Performance optimization and investigation of flow phenomena on tidal turbine blade airfoil considering cavitation and roughness. Appl. Ocean Res. 102463.

Vanilla, T.T., Benoit, A., Benoit, P., 2021. Hydro-elastic response of composite hydrofoil with FSI. Ocean Eng. 221, 108230.

Weisshaar, T.A., 2013. Morphing aircraft systems: historical perspectives and future challenges. J. Aircr. 50 (2), 337–353.

Woods, B.K., Parsons, L., Coles, A.B., Fincham, J.H., Friswell, M.I., 2016. Morphing elastically lofted transition for active camber control surfaces. Aerosp. Sci. Technol. 55, 439–448.

Young, Y.L., Motley, M.R., Barber, R., Chae, E.J., Garg, N., 2016. Adaptive composite marine propulsors and turbines: progress and challenges. Appl. Mech. Rev. 68 (6), 060803.

Zaresharif, M., Ravelet, F., Kinahan, D.J., Delaure, Y.M., 2021. Cavitation control using passive flow control techniques. Phys. Fluids 33 (12), 121301.